ORIGINAL PAPER

Zinc-, cadmium-, and mercury-containing one-dimensional tetraphenylporphyrin arrays: a DFT study

Ulises Jiménez Castillo · Ana E. Torres · Serguei Fomine

Abstract Metal-free, Zn-, Cd-, and Hg-containing one-dimensional tetraphenylporphyrin arrays containing up to eight repeat units were modeled at the PBE/def2-SVP level of theory with D3 empirical dispersion correction. Two different configurations—face to face (F) and parallel displaced (P)—were detected, the latter being the most stable for all types of nanoarrays. According to the calculations, the binding that occurs in nanoarrays is mostly due to dispersion, with binding energies of 33–35 kcal/mol seen for the metal-free nanoarrays and energies of 37–40 kcal/mol for the metal-containing ones. The band gaps, estimated as the S0→S1 excitation energies and extrapolated to the infinite chain limit using the TD-CAM-B3LYP/def2-SVP model, were close to 2 eV; the band gap size was barely dependent on the nature of the metal and the number of repeat units in the nanoarray. The ionization potentials and electron affinities were greatly influenced by the number of repeat units due to delocalization of polarons across each nanoarray. Polaron delocalization and the related reorganization energies were clearly dependent on the nature of the metal. For the metal-free and Zn-containing nanoarrays, the reorganization energies for hole and electron transport decreased linearly with $1/n$, where n is the number of repeat units in the nanoaggregate. The reorganization energies therefore reach zero for an infinitely long chain. These energies for Cd- and Hg-containing nanoarrays were found to be one order of magnitude higher for both hole and electron transport due to the localization of polarons in these nanoarrays.

Keywords Porphyrin · DFT · Dispersion correction · Reorganization energy · Polarons

U. J. Castillo · A. E. Torres · S. Fomine (✉)
Instituto de Investigaciones en Materiales, Universidad Nacional Autónoma de México, Apartado Postal 70-360, CU, Coyoacán, Mexico, DF 04510, México
e-mail: fomine@servidor.unam.mx

Introduction

Porphyrins are multifunctional molecules that mostly occur as complexes with metal ions, where nitrogen atoms in the porphyrins interact with the metal ions. The fortuitous combination of the redox properties of the metal and the rigid planar aromatic structure of the porphyrin allows such complexes to play important roles in oxygen and electron transfer, as well as in light-harvesting processes (as metalloproteins) [1–5].

Therefore, ever since the crystal structure of porphyrin was first solved [6], the number of papers describing the chemical and physical properties of porphyrins has grown exponentially, feeding fields related to the development of new synthetic techniques [7], potential applications of porphyrins in solar cells [8–11], molecular recognition [12–14], catalysis [15], electrochemistry [16], sensors [17, 18], data storage [19], and optoelectronics [20–26]. Porphyrins are able to self-assemble both in solution and in the solid state, forming one-, two-, or three-dimensional structures due to coordination, hydrogen bonding, and π–π stacking. It was recently demonstrated that submicrometer one-dimensional self-assembled porphyrin architectures can be obtained [27, 28]. Although numerous theoretical studies of the interactions of porphyrins and metalloporphyrins with electron acceptors have been published, there has been little research on porphyrin–porphyrin interactions [29, 30], and no detailed reports focusing on multiple porphyrin–porphyrin complexes. There are a few studies describing the electronic structures and transport properties of one-dimensional arrays of closely related phthalocyanines [31–33]. It was recently shown that dispersion interactions dominate in fullerene/porphyrin complexes and nanoarrays [34]. Therefore, dispersion interactions must be taken into account when modeling porphyrin complexes. For large systems involving multiple porphyrin molecules, meaning that the application of wavefunction-based methods is prohibitively expensive, DFT with explicit or

implicit dispersion correction is the only modeling method available.

Computational details

All geometry optimizations and energy calculations for tetraphenylporphyrin arrays containing up to eight porphyrin units were carried out using the PBE [35, 36] functional and the def2-SVP basis set with the resolution of identity and multipole accelerated resolution of identity approximations, as implemented in the TURBOMOLE 6.4 code [37]. The D3 empirical dispersion correction was used for all calculations [38]. No symmetry restrictions were imposed during the optimizations. Restricted and unrestricted DFT were used for the closed- and open-shell systems, respectively. Porphyrin nanoarrays are denoted nTPP-M, where n is the number of tetraphenylporphyrin units in the nanoarray and M is the metal species. A plus or minus symbol can also appear at the end of this notation, indicating the presence of a cation radical or an anion radical, respectively. Although neither experimental nor theoretical data on the stacking energies of tetraphenylporphyrin are available, the method applied accurately reproduces the interaction energy of the C_{60}/tetraphenylporphyrin complex
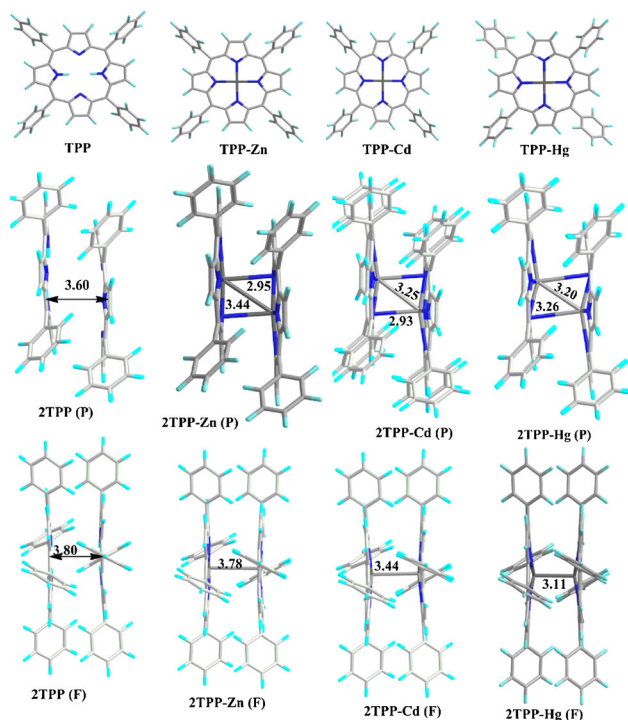

Fig. 1 PBE-D3/def2-SVP optimized geometries of the face-to-face (F) and parallel-displaced (P) nTPP and nTPP-M dimers, as well as those of the corresponding monomers. Distances are in Å

Table 1 Total binding energies (E_{tot}) calculated using the PBE+D3 model, and the corresponding contributions from the dispersion energy (E_{disp}, in kcal/mol). The S0→S1 excitation energies (eV) of the studied nanoaggregates, as calculated using the TD-PBE (E_{pbe}), TD-CAM-B3LYP (E_{cam}), and ADC(2) (E_{adc}) methods, are also shown

Complex	E_{tot}	E_{disp}	E_{pbe}	E_{cam}	E_{adc}
TPP	–	–	1.98	2.03	2.09
2TPP	36.6 (33.6)[b]	41.2 (37.8)[b]	1.65	1.99	1.89
4TPP	105.7 (35.2)	129.0 (43.0)	1.55	1.95	1.84
6TPP	175.4 (35.1)	215.5 (43.1)	1.51	1.95	-
8TPP	245.2 (35.0)	304.6 (43.5)	1.49	1.94	-
nTPP[a]	–	–	1.43	1.91	-
TPP-Zn	–	–	2.12	2.22	2.34
2TPP-Zn	43.5 (36.5)[b]	48.7 (38.7)[b]	1.78	2.16	2.12
4TPP-Zn	123.1 (41.0)	149.1 (49.7)	1.66	2.12	–
6TPP-Zn	202.8 (40.6)	249.7 (49.9)	1.58	2.11	–
8TPP-Zn	282.4 (40.3)	348.0 (49.7)	1.55	2.11	
nTPPZn[a]	–	–	1.46	2.11	
TPP-Cd	–	–	1.99	2.17	2.29
2TPP-Cd	43.4 (37.4)[b]	46.8 (40.0)[b]	1.70	2.11	2.12
4TPP-Cd	124.9 (41.6)	151.5 (50.5)	1.31	2.02	–
6TPP-Cd	204.7 (40.9)	257.8 (51.6)	1.12	2.01	–
8TPP-Cd	284.2 (40.6)	362.4 (51.8)	1.06	2.01	–
nTPPCd[a]	–	–	0.88	2.01	
TPP-Hg	–	–	1.23	2.16	1.70
2TPP-Hg	42.02 (38.1)[b]	45.3 (40.5)[b]	1.41	2.09	2.08
4TPP-Hg	121.8 (40.6)	146.6 (48.9)	1.26	2.05	-
6TPP-Hg	200.8 (40.2)	250.2 (50.1)	1.18	2.02	-
8TPP-Hg	279.1 (39.9)	351.8 (50.3)	1.14	2.02	-
nTPPHg[a]	–	–	1.02	2.02	

[a] Extrapolated to an infinitely long chain

[b] Binding energy for the F dimer configuration

estimated at the scaled opposite spin second-order Møller–Plesset (SOS-MP2) level of theory extrapolated to the basis set limit (27.0 vs. 31.5 kcal/mol) [39]. Both the C_{60}/tetraphenylporphyrin and tetraphenylporphyrin/tetraphenylporphyrin complexes show strong contributions from dispersion interactions to the total interaction energy, and if the method performs reasonably well for one system, it would be expected to do so for another. Metal-free, Zn-, Cd-, and Hg-containing tetraphenylporphyrin arrays were investigated. S0→S1 excitation energies extrapolated to an infinite number of repeat units were used as estimates for the band-gap energies of the nanoarrays. S0→S1 excitation energy calculations were carried out at the time-dependent (TD) CAM-B3LYP/def2-SVP [40], TD-PBE/def2-SVP, and RI-ADC(2)/def2-SVP levels of theory [41]. The resolution of identity second-order algebraic diagrammatic construction (RI-
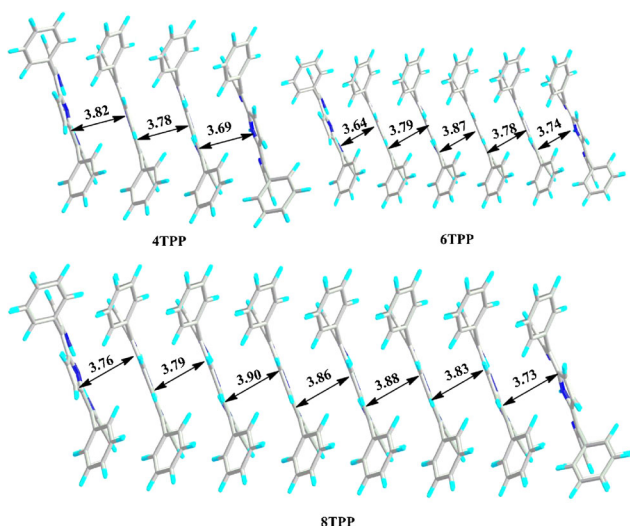
Fig. 2 PBE-D3/def2-SVP-optimized geometries of the P configurations of *n*TPP nanoarrays. Distances are in Å

Fig. 4 PBE-D3/def2-SVP-optimized geometries of the P configurations of *n*TPP-Cd nanoarrays. Distances are in Å

ADC(2)) method was used for the monomers, dimers, and 4TPP. All TD-CAM-B3LYP calculations were performed using the Gaussian 09 code [42].

Results and discussion

Geometry and binding energy

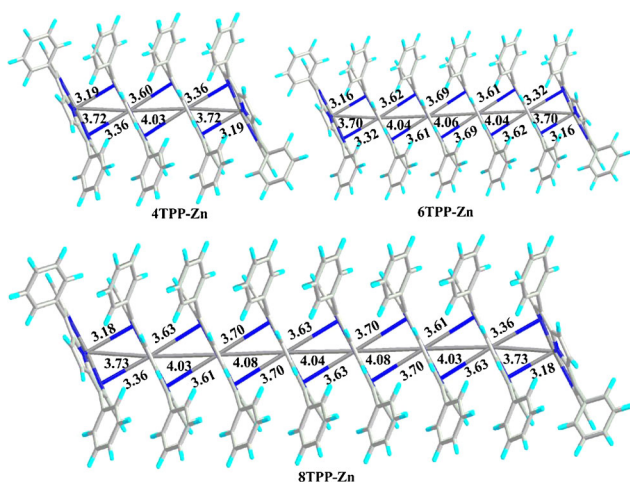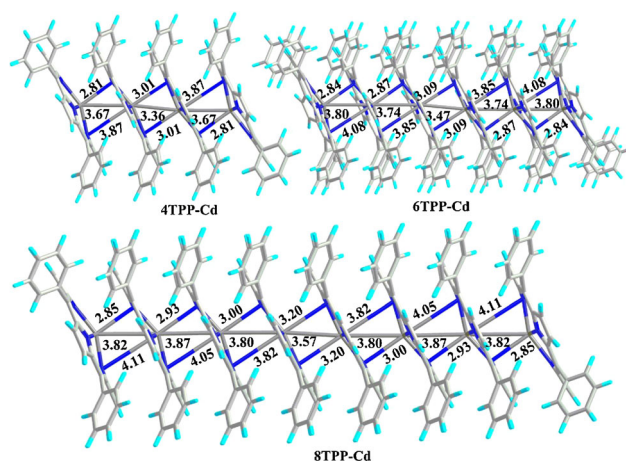Two types of alignments have been observed for *n*TPP and *n*TPP-M dimers: face to face (F) and parallel displaced (P). Figure 1 shows the optimized geometries of the corresponding dimers.

The binding energies of the complexes are listed in Table 1. For all of the dimers, the P complex was found to be more stable than the F complex. The difference in the calculated binding energies of the F and P dimers is about 3 kcal/mol for pure 2TPP; it increases to 7 kcal/mol for 2TPP-Zn, but it drops to 6 and 4 kcal/mol for 2TPP-Cd and 2TPP-Hg, respectively. The interplane distances are notably shorter in the P complexes than in the F complexes (Fig. 1), except for Hg-containing ones. Actually, a similar situation has already been reported for lithium phthalocyanine dimers, where the most stable dimer configuration is the parallel displaced one [32].
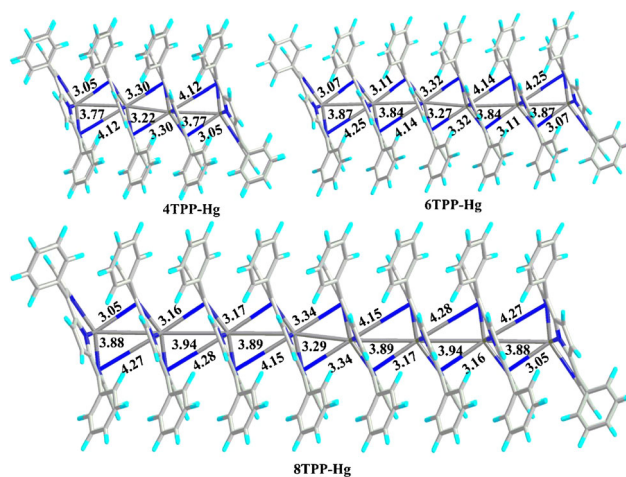

Fig. 3 PBE-D3/def2-SVP-optimized geometries of the P configurations of *n*TPP-Zn nanoarrays. Distances are in Å

Fig. 5 PBE-D3/def2-SVP-optimized geometries of the P configurations of *n*TPP-Hg nanoarrays. Distances are in Å

Each metal ion in a P dimer is coordinated with a nitrogen from the adjacent macrocycle, thus increasing the binding energy. Even metal–metal distances are shorter in P dimers than in F dimers. This additional interaction of each metal center with a nitrogen atom from the adjacent porphyrin macrocycle is reflected in an increased binding energy for the metal-containing dimer than for the corresponding metal-free dimer. The binding energy increases from 36.6 kcal/mol for the P dimer of 2TPP to 43.5 kcal/mol for the P dimer of 2TPP-Zn, and from 33.6 to 36.5 kcal/mol for the corresponding F dimers. A similar trend can be observed for other dimers, with the metal center increasing the binding energy for both types (P and F) of dimers (Table 1). As seen in Fig. 1, the metal–metal distances decrease for both types of complexes (P and F) upon switching from 2TPP-Zn to 2TPP-Hg because there is a stronger preference for Hg to interact with another

Hg atom rather than with nitrogen than there is for Zn to interact with another Zn atom rather than with nitrogen. Nitrogen is a relatively hard base, and Zn is a harder metal center than Hg, which leads to the decreased preference of Hg for participating in nitrogen–metal bonding. When assessing the contribution of the dispersion interactions to the binding energy (Table 1) it can be seen that the contribution from dispersion is higher than the binding energy calculated using the PBE energy plus dispersion. Therefore, only dispersion-based binding is present, and the interactions between macrocycles are repulsive at the pure DFT level. The dominance of the dispersion interaction is also a characteristic of porphyrin–fullerene complexes [34, 39]. The estimated porphyrin/porphyrin binding energy is higher than that of porphyrin/porphyrin/fullerene. Thus, the calculated binding energies for C60/TPP and C60/TPP-Zn complexes are 27 and

Fig. 6 Natural transition orbitals (NTO) calculated at the TD-CAM-B3LYP/def2-SVP level for the lowest electronic transition in *n*TPP nanoarrays. The hole is on the *left*; the particle is on the *right*
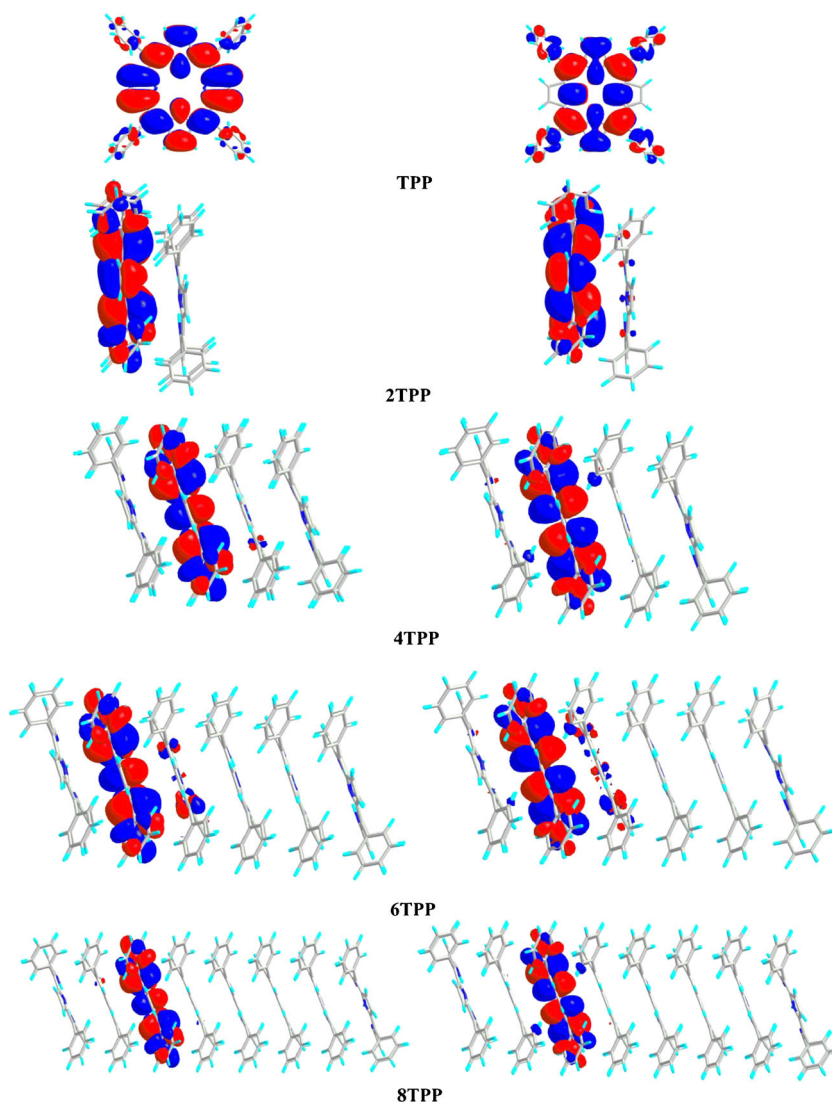
29.3 kcal/mol, respectively, compared to 36.6 and 43.5 kcal/mol for 2TPP and 2TPP-Zn [34]. These results are in line with experimental findings [43].

Large porphyrin nanoarrays containing up to eight repeat units were studied, but only for the most stable P conformation. As seen from Table 1, the binding energy per repeat unit does not depend on the number of repeat units in the nanoarray; it is only slightly smaller for tetramers, hexamers, and octamers than for the dimers. The optimized geometries of these nanoarrays are shown in Figs. 2, 3, 4, 5. While the trends in the interplane and metal–metal distances observed for the dimers are also maintained for the tetramers, hexamers, and octamers the values of these parameters are slightly larger for the tetramers, hexamers, and octamers compared to the dimers. The metal–metal distances in the nTPP-Zn series are

larger than those in the nTPP-Cd and nTPP-Hg series due to the preferences discussed above.

The porphyrin cycle of a metalloporphyrin is essentially planar, since metal–N interactions make it relatively rigid and difficult to deform. However, porphyrin itself is less rigid, and two closely positioned hydrogen atoms separated by only 2.1 Å distort the planarity of the porphyrin cycle. The significant nonplanarity of the porphyrin cycles in nTPPs makes it difficult to determine exact values for the interplane distances in these systems; only approximate values can be obtained.

Excited-state properties

The results of band-gap calculations for the nanoarrays are shown in Table 1.

Fig. 7 Natural transition orbitals (NTO) calculated at the TD-CAM-B3LYP/def2-SVP level for the lowest electronic transition in nTPP-Zn nanoarrays. The hole is on the *left*; the particle is on the *right*
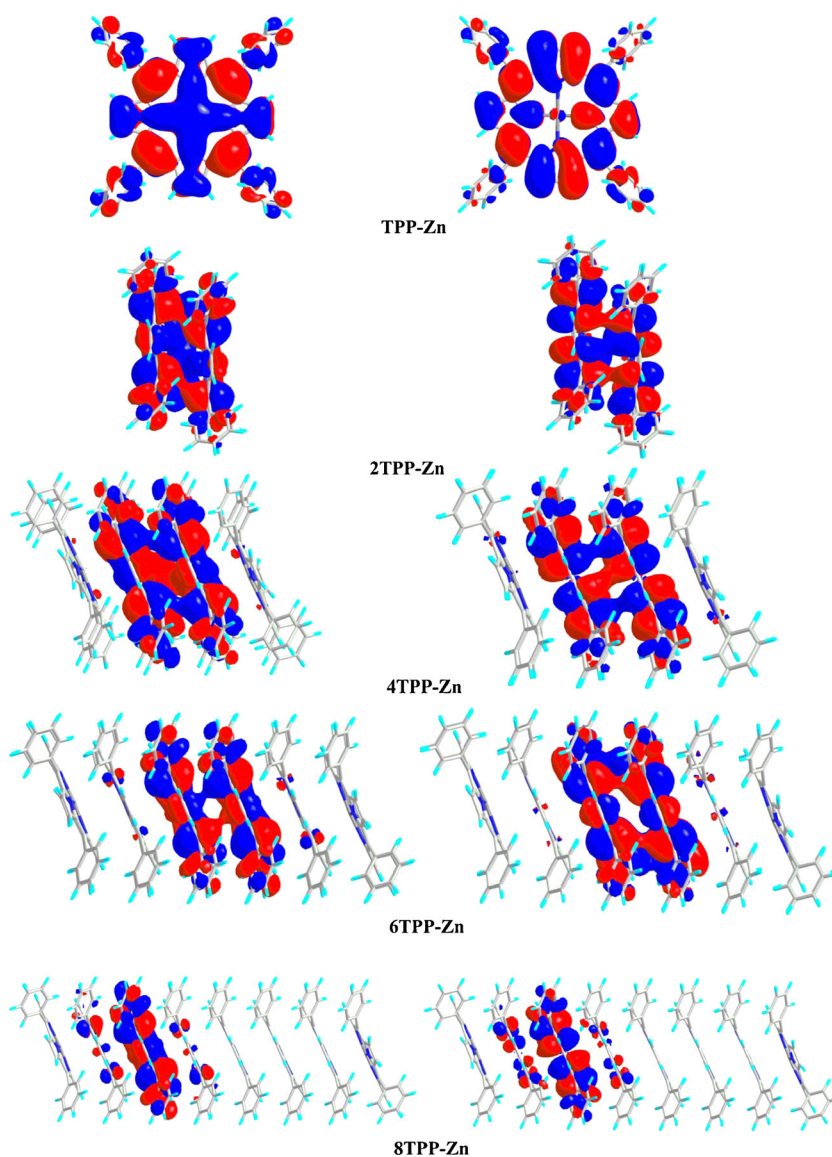
It is well known that pure functionals tend to underestimate the excitation energies of electronic transitions with significant charge-transfer (CT) contributions [44], whereas the CAM-B3LYP functional (based on long-range correction of the exchange potential) correctly treats CT transitions. The ADC(2) method is a wavefunction-based method, so it also gives correct results for CT transitions.

The TD-PBE/def2-SVP model accurately reproduces the experimental results for TPP and TPP-Zn long-wave absorption in toluene (TPP) and the gas phase (TPP-Zn, TPP-Cd) (1.97, 2.09, 2.03 (exp) vs. 1.98, 2.12, 1.99 eV, respectively) [45], and very similar results are afforded by the CAM-B3LYP/def2-SVP and ADC(2)/def2-SVP models (see Table 1). All of these methods predict that the S0→S1 excitation energy decreases with n for the nTPP and nTPP-M nanoarrays. The S0→S1 excitation energy increases slightly from nTPP to nTPP-Zn and then decreases for nTPP-Cd and nTPP-Hg nanoarrays. The difference between the S0→S1

energy predicted using TD-PBE on the one hand and that predicted using CAM-B3LYP or ADC(2) on the other increases with n. Although ADC(2) data are only available for the monomers, dimers, and metal-free tetramers, they can be considered a benchmark for TD-DFT methods. As seen in Table 1, the difference between the TD-CAM-B3LYP data and the ADC(2) data does not exceed 0.12 eV, while TD-PBE tends to produce S0→S1 energies that are notably lower than those afforded by the TD-CAM-B3LYP and ADC(2) methods for long nanoarrays.

To understand the differences observed between the TD-PBE excitation energies and those obtained with CAM-B3LYP and ADC(2), natural transition orbitals (NTO) were generated (Figs. 6, 7, 8, 9). It is apparent that the hole and particle orbitals are very similar for small nanoarrays, but they differ for larger nanoaggregates, in line with the increasing CT character of the electronic transition. This effect leads to the underestimation of S0→S1 energies when applying the TD-PBE method to large nanoarrays. The TD-CAM-B3LYP and

Fig. 8 Natural transition orbitals (NTO) calculated at the TD-CAM-B3LYP/def2-SVP level for the lowest electronic transition in nTPP-Cd nanoarrays. The hole is on the *left*; the particle is on the *right*
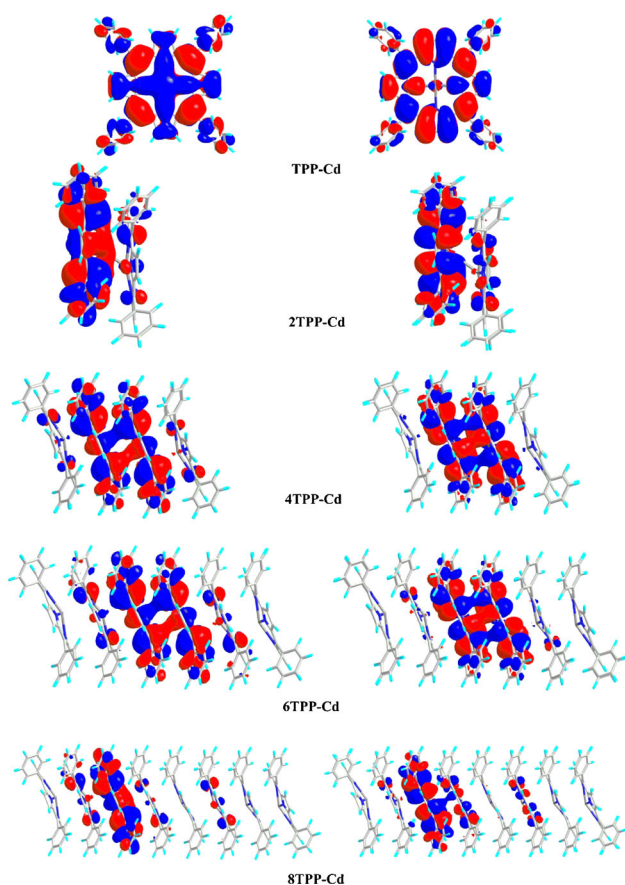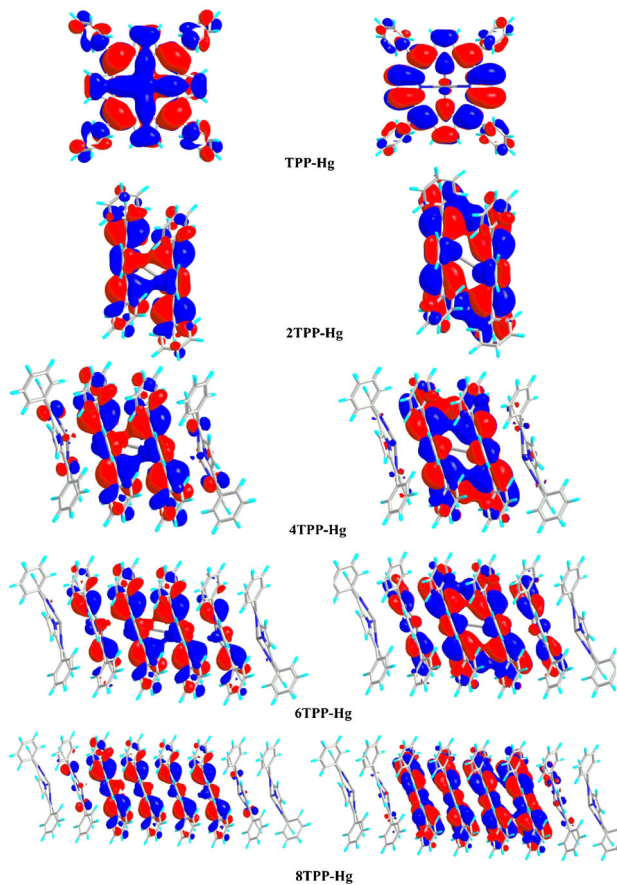

Fig. 9 Natural transition orbitals (NTO) calculated at the TD-CAM-B3LYP/def2-SVP level for the lowest electronic transition in nTPP-Hg nanoarrays. The hole is on the *left*; the particle is on the *right*

ADC(2) methods correctly treat CT states and produce similar results. Therefore, TD-CAM-B3LYP S0→S1 excitation energies are reasonable approximations to the band gaps of the nanoaggregates. It can be predicted on the basis of TD-CAM-B3LYP calculations that the band gap is close to 2 eV for infinite TPP arrays. The presence of metal ions barely affects this value, as the atomic orbitals of the metal ions barely participate in the NTOs. It is worth noting that a similar trend was observed for stacking metal and metal-free phthalocyanine iodides [33]. On the other hand, the nanoaggregate band gap decreases with the number of repeat units for all nanoaggregates (Table 1), although this decrease does not exceed 0.2 eV for the infinite chain (extrapolated).

Ionization potentials, electron affinities, and reorganization energies

Unlike the lowest excitation energy, which barely depends on the length of the nanoarray, the ionization potential (IP) and the electron affinity (EA) significantly depend on the n value of the nanoarray (Table 2), suggesting that both positive charge and negative charge are delocalized over the entire nanoaggregate. Thus, 8TPP and 8TPP-M nanoarrays have IP values of ~5 eV, which is very similar to the reported IP_a of polythiophene [46], while the extrapolated IP values for an infinitely long chain are 0.4–0.5 eV lower. EA increases with n for nanoaggregates, reaching 2.3–2.7 eV for an infinitely long chain, which is comparable to that of C_{60} [47]. The nature of the metal ion has a small but perceptible impact on IP and EA. As seen in Table 2, the metal-containing nanoaggregates show lower IPs and higher EAs than the corresponding metal-free nanoaggregates, and this effect is most pronounced for Cd and Hg due to their higher polarizabilities than Zn.

Figures 10, 11, 12, 13 show polaron delocalization in cation and anion radicals of nanoarrays, respectively. In a polaron, the charge is associated with an unpaired electron, so polaron delocalization can be visualized as unpaired electron density. As seen in Figs. 10–13, polaron cations are delocalized uniformly over the nitrogen atoms and the methyne carbons of the TPP units in nTPP and nTPP-Zn nanoarrays, explaining the decrease in IP with the size of the nanoaggregate. Phenyl substituents and Zn ions of Zn-containing nanoaggregates do not participate to a significant degree in the delocalization of polaron cations. For TPP-Cd and 2TPP-Cd, the delocalization of the polaron cation occurs in a similar way to that seen in nTPP and nTPP-Zn, while significant delocalization over the Hg center's d orbital is observed for TPP-Hg and 2TPP-Hg. For longer nanoaggregates containing Cd and Hg ions, the polaron cation

is more localized than it is in nTPP and nTPP-Zn, as seen in Figs. 12 and 13. For 8TPP-Cd and 8TPP-Hg, the polaron cation is mostly distributed over the terminal and four inner macrocycles. Polaron cation delocalization in tetramers and hexamers differs from that present in Cd- and Hg-containing systems. In the cases of 4TPP-Hg and 6TPP-Hg, the polaron is delocalized uniformly over the entire nanoaggregate, while for 4TPP-Cd and 6TPP-Cd, the polaron cation is localized mostly on terminal macrocycles. It is worth noting that, in nTPP-Hg nanoaggregates, a significant proportion of the unpaired polaron density is delocalized over d orbitals of Hg atoms (Fig. 13), in contrast to all other metal-containing cation radicals, where the central metal atom barely participates in the delocalization of the cation radical.

The delocalization patterns of polaron anions in nTPP and nTPP-Zn are similar to those seen for polaron cations (Figs. 10 and 11): the polaron anions are delocalized over the nitrogen atoms and methyne carbons of the TPP units, with the metal centers barely participating. For both nTPP and nTPP-Zn,

Table 2 Adiabatic (a) and vertical (v) ionization potentials (IP), electron affinity (EA), and reorganization energies for hole (λ_+) and electron (λ_-) transport

| Complex	IP_a	EA_a	IP_v	EA_v	λ_+	λ_-
TPP	6.07	1.56	6.12	1.48	0.09	0.12
2TPP	5.66	1.75	5.69	1.72	0.05	0.07
4TPP	5.29	1.94	5.31	1.92	0.04	0.04
6TPP	5.11	2.05	5.12	2.03	0.04	0.03
8TPP	4.97	2.12	4.98	2.11	0.03	0.02
nTPP	4.55	2.33	–	–	0.0	0.00
TPP-Zn	6.11	1.48	6.16	1.42	0.09	0.13
2TPP-Zn	5.72	1.73	5.76	1.69	0.08	0.09
4TPP-Zn	5.34	1.93	5.38	1.90	0.07	0.05
6TPP-Zn	5.16	2.04	5.18	2.02	0.04	0.04
8TPP-Zn	5.00	2.12	5.04	2.10	0.05	0.03
nTPPZn	4.52	2.36	–	–	-	0.00
TPP-Cd	6.00	1.67	6.13	1.51	0.17	0.23
2TPP-Cd	5.75	1.80	5.76	1.77	0.06	0.07
4TPP-Cd	5.27	2.15	5.31	2.06	0.07	0.09
6TPP-Cd	5.02	2.33	5.07	2.21	0.10	0.24
8TPP-Cd	4.87	2.42	4.93	2.29	0.13	0.27
nTPPCd	4.42	2.69			–	–
TPP-Hg	5.86	1.64	6.05	1.56	0.36	0.15
2TPP-Hg	5.45	1.82	5.68	1.78	0.41	0.08
4TPP-Hg	5.11	2.07	5.27	2.00	0.34	0.19
6TPP-Hg	4.92	2.23	5.06	2.12	0.32	0.31
8TPP-Hg	4.81	2.31	4.93	2.20	0.29	0.37
nTPPHg	4.48	2.55	–	–	–	-

most of the polaron is localized on the terminal macrocycles. While the distribution of polaron anion delocalization is very similar for all monomers and dimers, a difference is seen for long Cd- and Hg-containing nanoaggregates. As shown in Figs. 12 and 13, the polaron anions are localized mostly on the two inner macrocycles for these two nanoaggregates.

These differences among the nanoaggregates in their polaron delocalization distributions can be rationalized in terms of the electronegativity of the central metal ion. The electronegativity increases from Zn to Hg, which leads to an increase

in the EA of the nanoaggregate upon shifting from Zn- to Hg-containing nanoaggregates. Negative charge stabilization localizes the polaron anions at the centers of the Cd- and Hg-containing nanoaggregates. nTPP and nTPP-Zn are not capable of stabilizing their negative charge as effectively, so the most of the polaron is localized on the terminal macrocycles to reduce electronic repulsion. The opposite trend is observed for polaron cations, where a significant proportion of the unpaired density is localized on the terminal macrocycles.

The key to understanding the conductivity of the nanoaggregates is to characterize the structural factors that

Fig. 10 Delocalization of polaron cations and polaron anions in nTPP nanoarrays

TPP+

TPP-

2TPP+

2TPP-

4TPP+

4TPP-

6TPP+

6TPP-

8TPP+
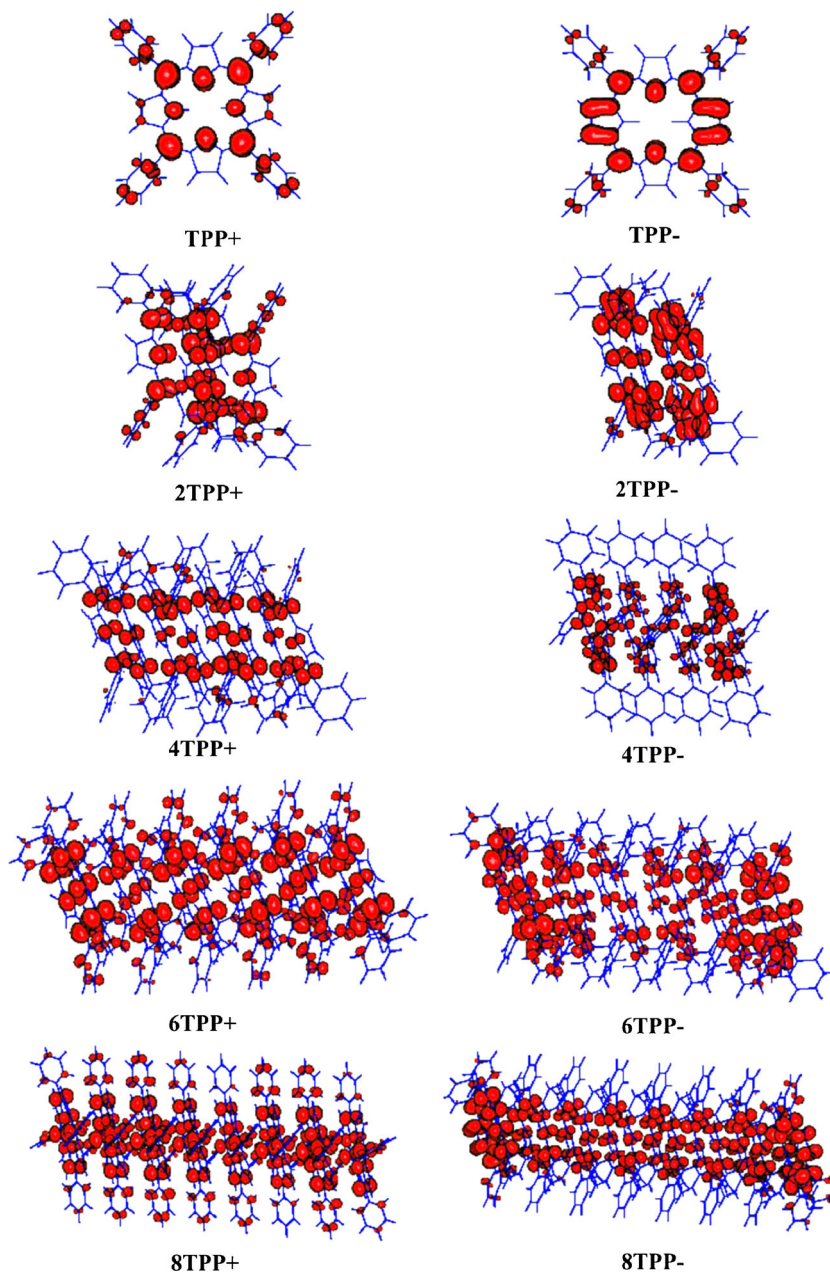
8TPP-

influence the charge transfer rate. Thus, it has been demonstrated that the solid-state hole mobility in arylamines is related to the internal reorganization energy λ [48–50]. The reorganization energy for hole mobility (λ_+) can be estimated as follows, as long as local vibronic coupling is dominant:

$$\lambda_+ = (E_n{}^+ - E_n) + (E_+{}^n - E_+).$$

Here, E_n and E_+ are the energies of the neutral and cationic species in their lowest-energy geometries, respectively, while $E_n{}^+$ and $E_+{}^n$ are the energies of the neutral and cationic species with the geometries of the cationic and neutral species, respectively. For electron transport, the reorganization energy is defined similarly:

$$\lambda_- = (E_n{}^- - E_n) + (E_-{}^n - E_-).$$

In this case, E_n and E_- are the energies of the neutral and the anionic species in their lowest-energy geometries, respectively, while $E_n{}^-$ and $E_-{}^n$ are the energies of the neutral and anionic species with the geometries of


Fig. 11 Delocalization of polaron cations and polaron anions in nTPP-Zn nanoarrays

TPP-Zn+   TPP-Zn-

2TPP-Zn+   2TPP-Zn-

4TPP-Zn+   4TPP-Zn-

6TPP-Zn+   6TPP-Zn-
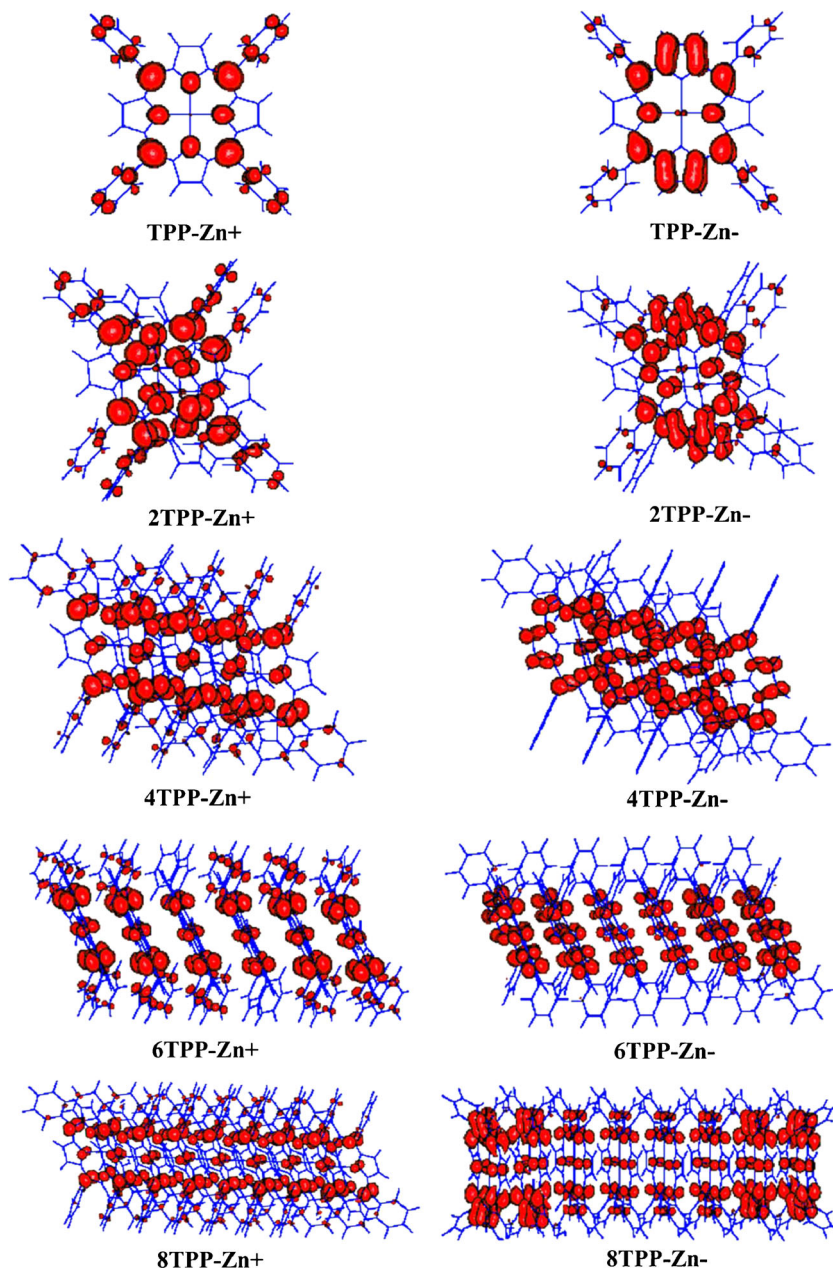
8TPP-Zn+   8TPP-Zn-

the cationic and the neutral species, respectively. Table 2 shows calculated λ_+ and λ_- values for nTPP. The relaxation energies for the nanoaggregates decrease with n. There is a linear correlation between λ and $1/n$ ($R^2 >$ 0.95) for both hole and electron transport. It is interesting that the same behavior was observed for the reorganization energies of polythiophene, polyselenophene [51], nTPP-Zn/C$_{60}$, and nTPP/C$_{60}$ nanoaggregates [34]. In the case of nTPP, λ_+ and λ_- reach 0 for an infinitely long chain; for nTPP-Zn, only λ_- reaches 0 for an infinitely long chain. As seen in Table 2 and Figs. 10–

13, the relaxation energies (λ) increase with polaron localization. Incorporating metal ions into the nanoarray increases the relaxation energy (increasingly so upon shifting from Zn- to Hg-containing nanoarrays). Therefore, all things being equal, the metal-free nanoarrays show the best charge mobilities for both electrons and holes. Long nTPP-Zn nanoarrays present lower reorganization energies for electron transport, while the lowest calculated reorganization energies are seen for polaron cations in Cd- and Hg-containing nanoarrays.

Fig. 12 Delocalization of polaron cations and polaron anions in nTPP-Cd nanoarrays

TPP-Cd+

TPP-Cd-

2TPP-Cd+

2TPP-Cd-

4TPP-Cd+

4TPP-Cd-

6TPP-Cd+

6TPP-Cd-

8TPP-Cd+

8TPP-Cd-
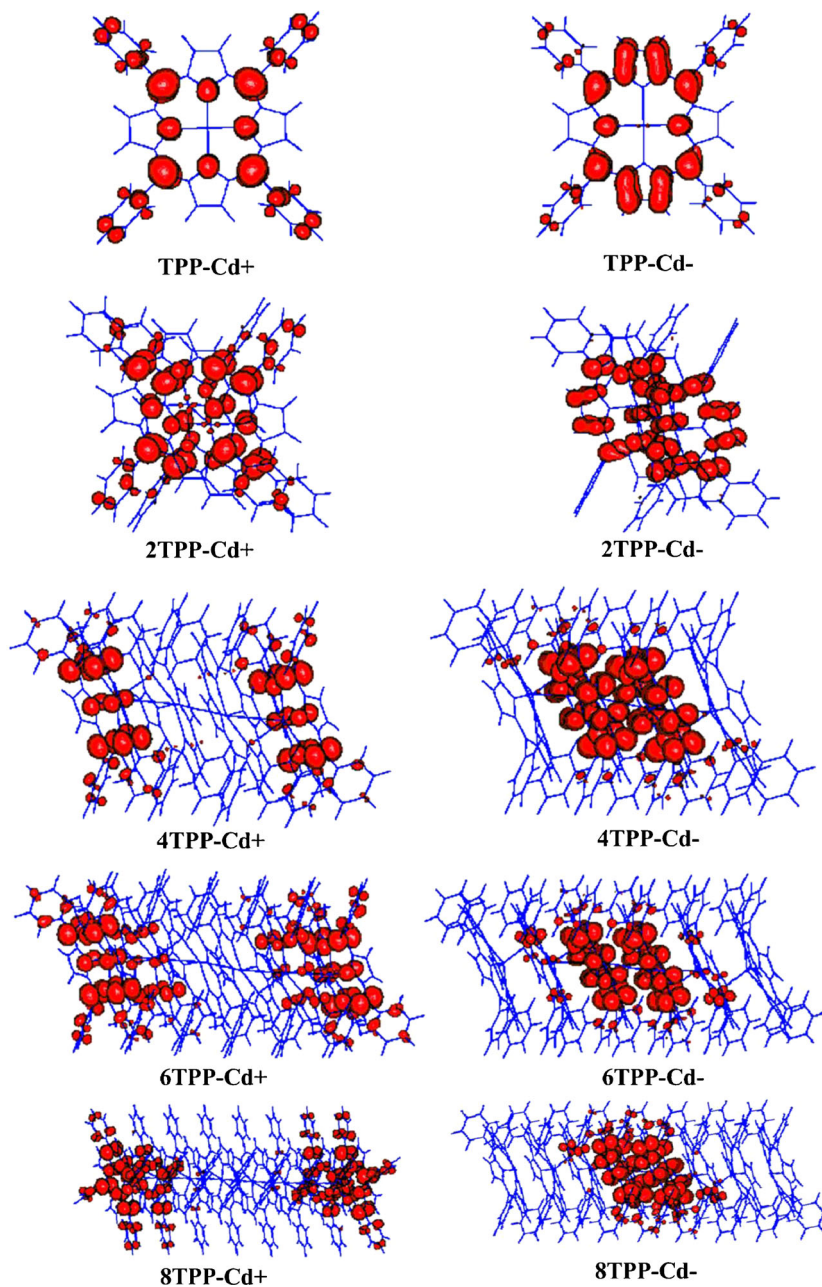
Conclusions

Two different configurations of metal-free, Zn-, Cd-, and Hg-containing one-dimensional tetraphenylporphyrin arrays were studied: face to face and parallel displaced. The latter is the most stable for all of the types of nanoarrays investigated in the present work. The binding present in the nanoarrays was found to be purely due to dispersion; calculations carried out without dispersion correction showed only repulsive interactions. The band gaps were estimated as the S0→S1 excitation energies extrapolated to an infinitely long chain using three different methods: TD-PBE, TD-B3LYP, and ADC(2). The TD-PBE model was found to be inapplicable due to the significant CT character of the electronic transitions in the long nanoarrays. The band gaps were close to 2 eV in size, and the band gap size barely depended on the nature of the metal and the number of repeat units in the nanoarray. The ionization potential and electron affinity were greatly influenced by the number of repeat units in the nanoarray due to the delocalization of polarons over the nanoarray. The polaron delocalization distribution and the related reorganization energies were significantly affected by the nature of the metal.

Fig. 13 Delocalization of polaron cations and polaron anions in *n*TPP-Hg nanoarrays
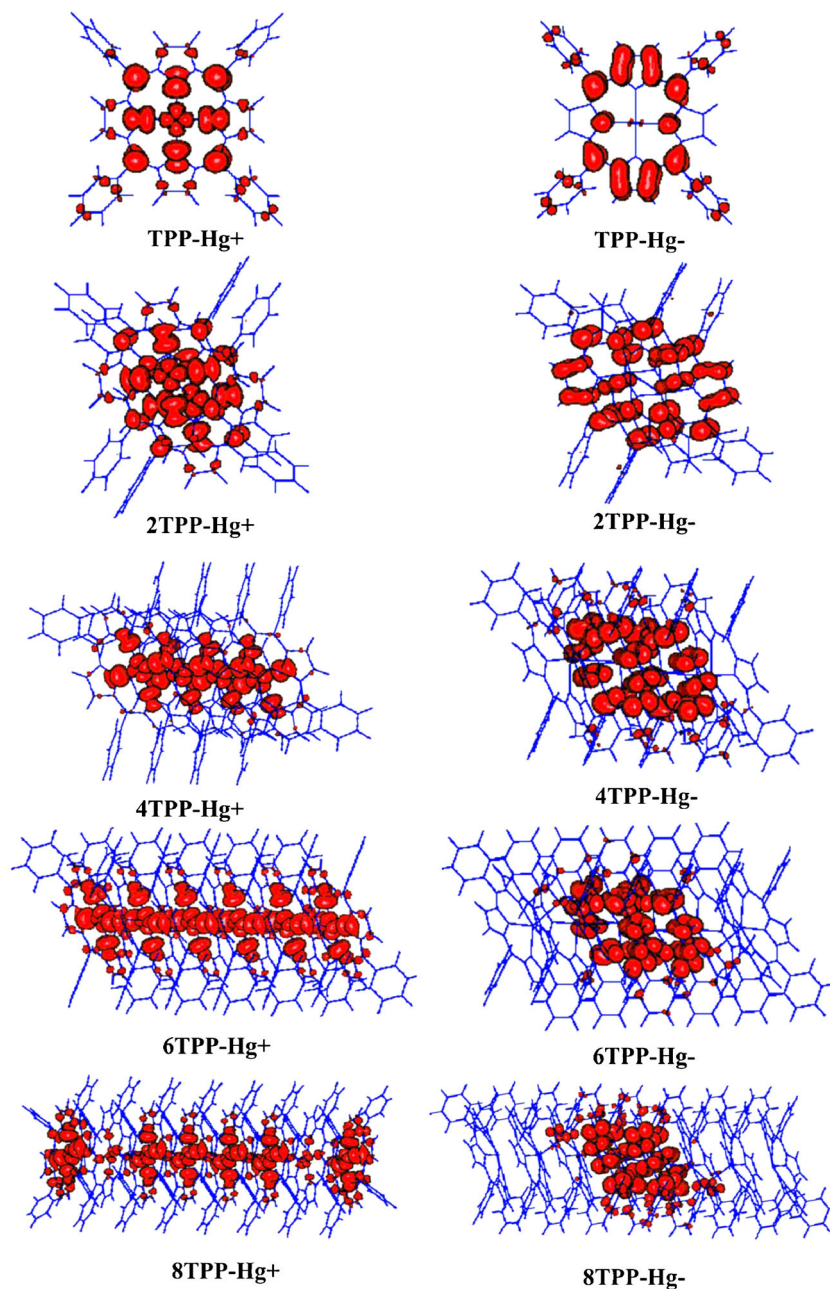
Thus, the reorganization energies for hole and electron transport in the metal-free and Zn-containing nanoarrays decreased linearly with $1/n$, where n is the number of repeat units in the nanoaggregate. The reorganization energies for both hole and electron transport are an order of the magnitude higher for the Cd- and Hg-containing nanoarrays than for the other nanoarrays, due to significant localization of the polarons in these nanoarrays.

References

1. Arai T, Kobata K, Mihara H, Fujimoto T, Nishino N (1995) A membrane-protein model: polypeptides with four α-helix bundle structure on 5,10,15,20-tetrakis[2-carboxymethoxy)phenyl]porphyrin. Bull Chem Soc Jpn 68:1989–1998

2. Arai T, Takei K, Nishino N, Fujimoto T (1996) Solvent-dependent chiral assembling of two zinc porphyrins in a zinc–free-base–zinc trimeric porphyrin array. Chem Commun 2133–2134

3. Dailey HA (1990) Biosynthesis of heme and chlorophylls. McGraw-Hill, New York

4. Geier GR, Sasaki T (1997) The design, synthesis and characterization of a porphyrin–peptide conjugate. Tetrahedron Lett 38:3821–3824

5. Rabanal F, Gibney BR, DeGrado WF, Moser CC, Dutton PL (1996) Engineering photosynthesis: synthetic redox proteins. Inorg Chim Acta 243:213–218

6. Crute M (1959) The crystal structure of nickel etioporphyrin II. Acta Crystallogr 12:24–28

7. Iengo E, Zangrando E, Alessio E (2006) Synthetic strategies and structural aspects of metal-mediated multiporphyrin assemblies. Acc Chem Res 39:841–851

8. Imahori H, Umeyama T (2009) Donor–acceptor nanoarchitecture on semiconducting electrodes for solar energy conversion. J Phys Chem C 113:9029–9039

9. Kelley RF, Shin WS, Rybtchinski B, Sinks LE, Wasielewski MR (2007) Photoinitiated charge transport in supramolecular assemblies of a 1,7,N,N'-tetrakis(zinc porphyrin)-perylene-3,4:9,10-bis(dicarboximide). J Am Chem Soc 129:3173–3181

10. Yoshimoto S, Itaya K (2007) Advances in supramolecularly assembled nanostructures of fullerenes and porphyrins at surfaces. J Porphyr Phthalocya 11:313–333

11. Nakamura Y, Aratani N, Osuka A (2007) Cyclic porphyrin arrays as artificial photosynthetic antenna: synthesis and excitation energy transfer. Chem Soc Rev 36:831–845

12. Guldi DM, Taieb H, Rahman GMA, Tagmatarchis N, Prato M (2005) Novel photoactive single-walled carbon nanotube–porphyrin polymer wraps: efficient and long-lived intracomplex charge separation. Adv Mater 17:871–875

13. Even P, Boitrel B (2006) Crown porphyrins. Coord Chem Rev 250:519–541

14. Diederich F, Felber B (2002) Supramolecular chemistry of dendrimers with functional cores. Proc Natl Acad Sci USA 99:4778–4781

15. Meunier B (1992) Metalloporphyrins as versatile catalysts for oxidation reactions and oxidative DNA cleavage. Chem Rev 92:1411–1456

16. Bonifazi D, Accorsi G, Armaroli N, Song FY, Palkar A, Echegoyen L, Scholl M, Seiler P, Jaun B, Diederich F (2005) Oligoporphyrin arrays conjugated to [60]fullerene: preparation, NMR analysis, and photophysical and electrochemical properties. Helvs Chim Acta 88:1839–1884

17. Facci P, Fontana MP, Dalcanale E, Costa M, Sacchelli T (2000) Molecular reorganization in Langmuir–Blodgett films of mesogenic Zn–porphyrin octaesters. Langmuir 16:7726–7730

18. Natale CD, Paolesse R, Macagnano A, Nardis S, Martinelli E, Dalcanale E, Costa M, D'Amico A (2004) Sensitivity–selectivity balance in mass sensors: the case of metalloporphyrins. J Mater Chem 14:1281–1287

19. Mammana A, D'Urso A, Lauceri R, Purrello R (2007) Switching off and on the supramolecular chiral memory in porphyrin assemblies. J Am Chem Soc 129:8062–8063

20. Ahn TK, Kim KS, Kim DY, Noh SB, Aratani N, Ikeda C, Osuka A, Kim D (2006) Relationship between two-photon absorption and the π-conjugation pathway in porphyrin arrays through dihedral angle control. J Am Chem Soc 128:1700–1704

21. Hoeben FJM, Wolffs M, Zhang J, De Feyter S, Leclère P, Schenning APHJ, Meijer EW (2007) Influence of supramolecular organization on energy transfer properties in chiral oligo(p-phenylene vinylene) porphyrin assemblies. J Am Chem Soc 129:9819–9828

22. Kurotobi K, Kim KS, Noh SB, Kim D, Osuka A (2006) A quadruply azulene-fused porphyrin with intense near IR absorption and a large two-photon absorption cross section. Angew Chem Int Ed 45:3944–3947

23. Kim D, Osuka A (2004) Directly linked porphyrin arrays with tunable excitonic interactions. Acc Chem Res 37:735–745

24. Hwang IW, Kamada T, Ahn TK, Ko DM, Nakamura T, Tsuda A, Osuka A, Kim D (2004) Porphyrin boxes constructed by homochiral self-sorting assembly: optical separation, exciton coupling, and efficient excitation energy migration. J Am Chem Soc 126:16187–16198

25. Aimi J, Oya K, Tsuda A, Aida T (2007) Chiroptical sensing of asymmetric hydrocarbons using a homochiral supramolecular box from a bismetalloporphyrin rotamer. Angew Chem Int Ed 46:2031–2035

26. Tsuda A, Sakamoto S, Yamaguchi K, Aida T (2003) Novel supramolecular multicolor thermometer by self-assembly of a π-extended zinc porphyrin complex. J Am Chem Soc 125:15722–15723

27. Hu JS, Guo YG, Liang HP, Wan LJ (2005) Three-dimensional self-organization of supramolecular self-assembled porphyrin hollow hexagonal nanoprisms. J Am Chem Soc 127:17090–17095

28. Fathalla M, Neuberger A, Li S-C, Schmehl R, Diebold U, Jayawickramarajah J (2010) Straightforward self-assembly of porphyrin nanowires in water: harnessing adamantane/β-cyclodextrin interactions. J Am Chem Soc 132:9966–9967

29. Collman JP, Arnold HJ, Weissman KJ, Burton JM (1994) Heterometallic mixed triad multiple bonds in metal–porphyrin dimers. J Am Chem Soc 116:9761–9762

30. Collman JP, Arnold HJ (1993) Multiple metal–metal bonds in $4d$ and $5d$ metal–porphyrin dimers. Acc Chem Res 26:586–592

31. Krauss TN, Barrena E, Lohmüller T, Kelsch M, Breitling A, van Aken PA, Spatz JP, Dosch H (2009) One-dimensional phthalocyanine nanostructures directed by gold templates. Chem Mater 21:5010–5015

32. Sumimoto M, Kawashima Y, Yokogawa D, Hori K, Fujimoto H (2011) Theoretical study on the molecular structures of X-, α-, and β-types of lithium phthalocyanine dimer. J Comp Chem 32:3062–3067

33. Chen S, Ma J (2009) Charge transport in stacking metal and metal-free phthalocyanine iodides. Effects of packing, dopants, external electric field, central metals, core modification, and substitutions. J Comp Chem 30:1959–1972

34. Jiménez U, Guadarrama P, Fomine S (2013) Large face to face tetraphenylporphyrin/fullerene nanoaggregates. A DFT study. Org Electron 14:2617–2627

35. Perdew JP, Burke K, Ernzerhof M (1996) Generalized gradient approximation made simple. Phys Rev Lett 77:3865–3868

36. Perdew JP, Burke K, Ernzerhof M (1997) Errata: Generalized gradient approximation made simple. Phys Rev Lett 78:1396

37. Furche F et al. (2012) TURBOMOLE V6.4. University of Karlsruhe/ Forschungszentrum Karlsruhe, Karlsruhe. http://www.turbomole.com

38. Grimme S, Antony J, Ehrlich S, Krieg H (2010) A consistent and accurate ab initio parametrization of density functional dispersion correction (DFT-D) for the 94 elements H–Pu. J Chem Phys 132:154104

39. Jung Y, Head-Gordon M (2006) A fast correlated electronic structure method for computing interaction energies of large van der Waals complexes applied to the fullerene–porphyrin dimer. Phys Chem Chem Phys 8:2831–2840

40. Yanai T, Tew DP, Handy NC (2004) A new hybrid exchange– correlation functional using the Coulomb-attenuating method (CAM-B3LYP). Chem Phys Lett 393:51–57

41. Hättig C (2005) Structure optimizations for excited states with correlated second-order methods: CC2 and ADC(2). Adv Quant Chem 50:37–60

42. Frisch MJ et al. (2010) Gaussian 09, revision C.01. Gaussian, Inc., Wallingford

43. Boyd PDW, Reed CA (2005) Fullerene−porphyrin constructs. Acc Chem Res 38:235–242

44. Dreuw A, Head-Gordon M (2005) Single-reference ab initio methods for the calculation of excited states of large molecules. Chem Rev 105:4009–4037

45. Dolphin D (1978) The porphyrins: physical chemistry, vol 3, part A, 1st edn. Academic, London

46. Salzner U, Pickup PG, Poirier RA, Lagowski JB (1998) An accurate method for obtaining band gaps in conducting polymers using a DFT/ hybrid approach. J Phys Chem A 102:2572–2578 (and references therein)

47. Wang XB, Ding CF, Wang LS (1999) High resolution photoelectron spectroscopy of C60$^-$. Chem Phys 110:8217–8220

48. Lin BC, Cheng CP, Lao ZPM (2003) Reorganization energies in the transports of holes and electrons in organic amines in organic electroluminescence studied by density functional theory. J Phys Chem A 107:5241–5251

49. Malagoli M, Brédas JL (2000) Density functional theory study of the geometric structure and energetics of triphenylamine-based hole-transporting molecules. Chem Phys Lett 327:13–17

50. Sakanoue K, Motoda M, Sugimoto M, Sakaki S (1999) A molecular orbital study on the hole transport property of organic amine compounds. J Phys Chem A 103:5551–5556

51. Zade SS, Bendikov M (2008) Study of hopping transport in long oligothiophenes and oligoselenophenes: dependence of reorganization energy on chain length. Chem Eur J 14:6734–6741